Mater Renew Sustain Energy (2017) 6:10
DOI 10.1007/s40243-017-0094-4

ORIGINAL PAPER

Perovskite $Sr_{1-x}Ba_xW_{1-y}Ta_y(O,N)_3$: synthesis by thermal ammonolysis and photocatalytic oxygen evolution under visible light

Kenta Kawashima[1,2] · Mirabbos Hojamberdiev[1] · Christina Stabler[3] · Dragoljub Vrankovic[3] · Kunio Yubuta[4] · Ralf Riedel[3] · Kazunari Domen[5] · Katsuya Teshima[1,6]

Received: 9 February 2017 / Accepted: 2 May 2017 / Published online: 12 May 2017

Abstract To study the effect of partial Ba^{2+}-to-Sr^{2+} and/or Ta^{5+}-to-W^{4-6+} substitution on various properties of $SrW(O,N)_3$, cubic perovskite-type W- and/or Ta-based oxynitrides $Sr_{1-x}Ba_xW_{1-y}Ta_y(O,N)_3$, where $x,y = 0,0$; 0.25,0; 0.125,0.125; 0,0.25; and 1.1, were synthesized by ammonolyzing their corresponding oxide precursors under an NH_3 flow. The synthesized oxynitrides have highly porous structures and consist of small crystallites in the range of 53–630 nm and with specific surface areas in the range of 5.4–14.7 $m^2 \cdot g^{-1}$. Interestingly, the Ta^{5+}-to-$W^{4\sim6+}$ substitution in $SrW(O,N)_3$ can suppress the formation of reduced tungsten species during thermal ammonolysis. The weaker absorptions beyond 560 and 580 nm in the UV–Vis diffuse reflectance spectra, which correspond to reduced tungsten species, are observed in $SrW_{0.75}Ta_{0.25}(O,N)_3$ and $Sr_{0.875}Ba_{0.125}W_{0.875}Ta_{0.125}(O,N)_3$ compared to $SrW(O,N)_3$ and $Sr_{0.75}Ba_{0.25}W(O,N)_3$. The XPS results reveal that low-valent transition metal oxides, nitrides, and oxynitrides and/or tungsten metal are present on the surfaces of the as-synthesized oxynitrides. After 5 h of the photocatalytic oxygen evolution reaction, CoO_x-loaded $SrW_{0.75}Ta_{0.25}(O,N)_3$ exhibited the highest amount of evolved O_2 gas due to its higher specific surface area and lower concentration of intrinsic defects. During the photocatalytic reaction, the N_2 gas is also evolved because of the self-oxidation of oxynitrides consuming photo-generated holes. The estimated TONs of the oxynitride samples exceeded one, evidencing that the observed O_2 gas evolution reactions were catalytic. Accordingly, the photostability enhancement of oxynitrides reduces the loss of photo-generated charge carriers and increases their photocatalytic activity.

Graphical abstract

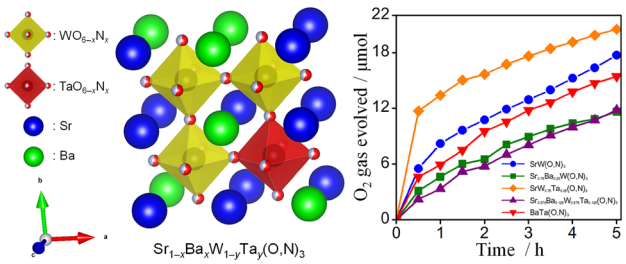

Keywords Water oxidation · Oxynitride perovskite · Visible light · Substitution

Electronic supplementary material The online version of this article (doi:10.1007/s40243-017-0094-4) contains supplementary material, which is available to authorized users.

✉ Kenta Kawashima
kawashimak2015@gmail.com

Katsuya Teshima
teshima@shinshu-u.ac.jp

1 Department of Environmental Science and Technology, Faculty of Engineering, Shinshu University, 4-17-1 Wakasato, Nagano 380-8553, Japan

2 McKetta Department of Chemical Engineering, The University of Texas at Austin, Austin, TX 78712, USA

3 Institut für Materialwissenschaft, Technische Universität Darmstadt, Jovanka-Bontschits-Strasse 2, 64287 Darmstadt, Germany

4 Institute for Materials Research, Tohoku University, 2-1-1 Katahira, Aoba-ku, Sendai 980-8577, Japan

5 Department of Chemical System Engineering, School of Engineering, The University of Tokyo, 7-3-1 Hongo, Bunkyo-ku, Tokyo 113-8656, Japan

6 Center for Energy and Environmental Science, Shinshu University, 4-17-1 Wakasato, Nagano 380-8553, Japan

Introduction

Artificial photocatalysis for solar water splitting has been regarded as a source for clean and sustainable fuel and chemical production [1–3]. To achieve efficient solar energy conversion, it is indispensable that the photon energy in the visible light range should be utilized for the photocatalytic reaction [4]. It is known from previous studies that the efficient photocatalysts, including transition and typical metal oxides, oxynitrides, and nitrides, contain metal cations of Ti^{4+}, Nb^{5+}, Ta^{5+}, or W^{6+} with d^0 electronic configuration and of Ga^{3+}, In^{3+}, Ge^{4+}, Sn^{4+}, or Sb^{5+} with d^{10} electronic configuration [5, 6]. In recent years, transition metal oxynitride perovskites with narrower band gaps and suitable band structures (e.g., $LaTiO_2N$ [7], $BaNbO_2N$ [8], $BaTaO_2N$ [9], $CaTaO_2N$ [10], $LaMg_{1/3}Ta_{2/3}O_2N$ [11], and so on) are regarded as an emerging class of inorganic materials that can effectively utilize solar energy for photocatalytic reactions. However, the previously reported photocatalytic activities of transition metal oxynitride perovskites are still not sufficient to realize practically the developed solar energy systems. Therefore, it is necessary to discover novel materials having a high potential for photocatalytic water splitting and to develop new strategies to improve the photocatalytic activities of transition metal oxynitride perovskites.

In our recent work, we have explored five tungsten-based oxynitride perovskites $AW(O,N)_3$, A = Sr, La, Pr, Nd, and Eu as novel materials for visible light-driven photocatalytic water oxidation [12]. Among the five samples, the CoO_x-loaded $SrW(O,N)_3$ exhibited higher photostability and photocatalytic O_2 evolution rate of 3.3 μmol h^{-1} due to the presence of active sites for O_2 evolution on the surfaces and absence of the intrinsic defects related to the partly filled 4f orbitals. Although the $SrW(O,N)_3$ photocatalyst has the potential for photocatalytic O_2 evolution reaction, it needs to be further improved by applying a novel strategy.

Regarding to the $AB(O,N)_3$-type materials, it was reported that the substitution of the A-site or B-site cation can improve the photocatalytic activity of $AB(O,N)_3$. For example, the $(La,Ca)Ti(O,N)_3$ crystals, which were synthesized by thermal ammonolysis of A-site-deficient $La_{1-x}TiO_{3.5-3x/2}$ precursor ($x = 0.05$) treated in an aqueous solution containing $Ca(NO_3)_2{\cdot}4H_2O$, showed higher activity for photocatalytic water oxidation (O_2 evolution rate: 40 μmol h^{-1}) compared with the pure $LaTiO_2N$ crystals (O_2 evolution rate: 22 μmol h^{-1}) due to their higher crystallinity and lower concentration of intrinsic defects (Ti^{3+}) that act as a recombination center for photoexcited electrons and holes [13]. The formation of Ti^{3+} was restrained by substituting La^{3+} with Sr^{2+} in $(La,Sr)TiO_2N$ because the lower-valent A-site cation may induce the oxidation of titanium [14]. On the other hand, introducing the tungsten species having $5d^1$ electronic configuration into the B-site of $BaTaO_2N$ showed an exceedingly effective impact on enhancing the photocatalytic water oxidation activity [15]. Furthermore, the CoO_x-loaded $BaNb_{1-x}Ta_xO_2N$ porous structures ($x = 0.50$) exhibited higher photocatalytic O_2 evolution rate (127.24 μmol in the first 2 h) than the CoO_x-loaded pure $BaNbO_2N$ porous structures (20.92 μmol in the first 2 h) owing to the high specific surface area and low density of structural defects [16]. As mentioned above, the photocatalytic activity of $AB(O,N)_3$ can be significantly enhanced by the exquisite combination of the substitutional elements and parent materials, which still has many untouched possibilities to explore.

In the present study, we have synthesized five Ba- and/or Ta-substituted strontium tungsten oxynitride perovskites $Sr_{1-x}Ba_xW_{1-y}Ta_y(O,N)_3$, where x,y = 0,0; 0.25,0; 0.125,0.125; 0,0.25; and 1.1, by thermal ammonolysis of their oxide precursor crystals. This study attempts to investigate the effect of partial Ba^{2+}-to-Sr^{2+} and/or Ta^{5+}-to- $W^{4\sim6+}$ substitution on the O/N ratio, band gap, and photocatalytic water oxidation activity of $SrW(O,N)_3$ photocatalyst.

Experiment

Growth of $Sr_{1-x}Ba_xW_{1-y}Ta_yO_{4-(1/2)y}$ and $Ba_5Ta_4O_{15}$ crystals

The $Sr_{1-x}Ba_xW_{1-y}Ta_yO_{4-(1/2)y}$, where x,y = 0,0; 0.25,0; 0,0.25; and 0.125,0.125, and $Ba_5Ta_4O_{15}$ crystals were synthesized by a solid-state reaction and KCl flux method with 10 mol % solute concentration, respectively. Reagent-grade $SrCO_3$ (≥ 95%, Wako), $BaCO_3$ (99.9%, Wako), WO_3 (≥ 95%, Wako), Ta_2O_5 (99.9%, Wako) and KCl (99.5%, Wako) were dry mixed manually in stoichiometric ratio using an agate mortar and a pestle. Continuously, each mixture (10 g) was placed in an alumina crucible and closed loosely with an alumina lid. The mixture-containing alumina crucible was heated at 1100 °C for 3 h at a heating rate of 100 °C h^{-1} for $Sr_{1-x}Ba_xW_{1-y}Ta_yO_{4-(1/2)y}$ or at 1000 °C for 10 h at a heating rate of 50 °C h^{-1} for $Ba_5Ta_4O_{15}$, cooled to 500 °C at a cooling rate of 150 °C h^{-1}, and then naturally cooled to room temperature. As for $Ba_5Ta_4O_{15}$, the flux-grown crystals were washed with deionized water to remove the remaining flux and then dried at 100 °C for 12 h in a drying oven.

Synthesis of $Sr_{1-x}Ba_xW_{1-y}Ta_y(O,N)_3$ and $BaTa(O,N)_3$ crystal structures

To obtain the $Sr_{1-x}Ba_xW_{1-y}Ta_y(O,N)_3$ and $BaTa(O,N)_3$ oxynitride crystal structures, 1.0 g of the as-synthesized $Sr_{1-x}Ba_xW_{1-y}Ta_yO_{4-(1/2)y}$ crystals were placed on an alumina plate and ammonolyzed at 900 °C for 10 h for $SrWO_4$ and $Sr_{0.75}Ba_{0.25}WO_4$, 30 h for $Sr_{0.875}Ba_{0.125}W_{0.875}Ta_{0.125}O_{3.9375}$, and 40 h for $SrW_{0.75}Ta_{0.25}O_{3.975}$, while 1.0 g of the flux-grown $Ba_5Ta_4O_{15}$ crystals were ammonolyzed at 950 °C for 40 h at a heating rate of 600 °C h^{-1} under an NH_3 flow (200 mL min^{-1}) in a vertical tubular furnace.

Characterization

X-ray powder diffraction (XRD) patterns were recorded on a Rigaku MiniflexII X-ray diffractometer (Cu Kα radiation ($\lambda = 1.5406$ Å)). The recorded XRD peak positions were calibrated using an unstressed Si powder standard with a *111* diffraction peak at 28.44°. The high-resolution scanning electron microscopy (SEM) observations were performed using a JSM-7600F scanning electron microscope (JEOL) attached with an energy-dispersive X-ray spectrometer (EDS). The ultraviolet–visible (UV–Vis) diffuse reflectance spectra were measured by a V-670 spectrophotometer (JASCO). The nitrogen and oxygen contents were determined by hot-gas extraction using a LECO TC-436 N/O analyzer (LECO Co.). The specific surface areas of the oxynitride samples were determined by the Brunauer, Emmett, and Teller (BET) method from the linear portion of the nitrogen gas adsorption isotherms measured at −196 °C using an Autosorb-1A (Quantachrome Instruments). The samples were preheated at 150 °C for 24 h under vacuum before the measurements. The surface chemical compositions and chemical states of elements of the synthesized oxynitrides were investigated using a JPS-9010MC X-ray photoelectron spectroscope (XPS, JEOL) with a non-monochromatic Mg Kα-excitation X-ray source. The C 1 s peak at 284.5 eV was used to calibrate the spectra.

Photocatalytic water oxidation activity test

The photocatalytic O_2 gas evolution reactions were performed in a glass cell attached to a closed gas circulation system connected to a gas chromatograph (GC-8A, TCD, Ar gas carrier, Shimadzu) equipped with a vacuum line. First, 100 mg of CoO_x-loaded oxynitride sample and 200 mg of La_2O_3 (as a pH buffer) were suspended in 300 mL of 10 mM $AgNO_3$ (> 99%, Wako) aqueous solution (as a sacrificial electron scavenger) in the glass cell under magnetic stirring. A 300 W Xe lamp with a cutoff filter ($\lambda > 420$ nm) was used as a visible light source and its light intensity was 11 mW cm^{-2} at 360 nm. The evolved O_2 and N_2 gases were detected by a GC. The CoO_x (2 wt % Co) nanoparticles as a cocatalyst for O_2 gas evolution were loaded by immersing the oxynitride samples in $Co(NO_3)_2{\cdot}6H_2O$ (> 99%, Wako) aqueous solution and heat treatment at 700 °C for 1 h under an NH_3 flow (200 mL min^{-1}) followed by heat treatment at 200 °C for 1 h in air.

The turnover numbers (TONs) for 5 h photocatalytic O_2 gas evolution reactions were estimated as the total moles of substrates (H_2O) consumed over the reaction per moles of active catalytic species (CoO_x) [17, 18]:

$$\mathrm{TON} = \frac{\text{number of moles of } H_2O}{\text{number of moles of } CoO_x} \quad (1)$$

It is known that the loaded cobalt oxide particles are mainly in the forms of CoO and Co_3O_4 [3]. For the calculation, assuming that the molar amount of CoO is the same as that of Co_3O_4 in the loaded cobalt oxide particles, CoO_x was accordingly regarded as $Co_2O_{2.5}$. The turnover frequencies (TOFs), the number of TONs per unit time of reaction, were determined using the following equation [18]:

$$\mathrm{TOF} = \frac{\mathrm{TON}}{\text{unit time of reaction}} \quad (2)$$

Results and discussion

Characterization of the synthesized oxide precursors and oxynitride perovskites

Figure 1 shows the XRD patterns of $Sr_{1-x}Ba_xW_{1-y}Ta_yO_{4-(1/2)y}$ and $Ba_5Ta_4O_{15}$ precursor crystals synthesized by a solid-state reaction. As shown in Fig. 1a, e, the XRD patterns of the samples are identical to that of a single-phase $SrWO_4$ (ICDD PDF# 08-0490) and $Ba_5Ta_4O_{15}$ (ICDD PDF# 72-0631) with tetragonal and hexagonal structures, respectively. The XRD patterns of the $Sr_{1-x}Ba_xW_{1-y}Ta_yO_{4-(1/2)y}$ ($x,y = 0.25,0$; $0,0.25$; and $0.125,0.125$) crystals mostly correspond to the tetragonal $SrWO_4$ phase, and the presence of minor $Sr_2Ta_2O_7$ (ICDD PDF# 72-0921) and some unidentified impurity phases were also detected (Fig. 1b–d). The formation of the $Sr_2Ta_2O_7$ phase evidences that the Ta^{5+}-substitution levels of 12.5 and 25% have already exceeded the substitution limit. On increasing the Ba^{2+}-substitution level from 0 to 25%, the main *112* diffraction peak of $SrWO_4$ at 27.65° in the recorded XRD patterns slightly shifted toward a lower 2θ angle because the unit cell volumes of the $Sr_{1-x}Ba_xW_{1-y}Ta_yO_{4-(1/2)y}$ crystals increased as a result of the increase of the ratio of larger Ba^{2+} ions ($r_{ionic} = 1.42$ Å: CN = 8) to

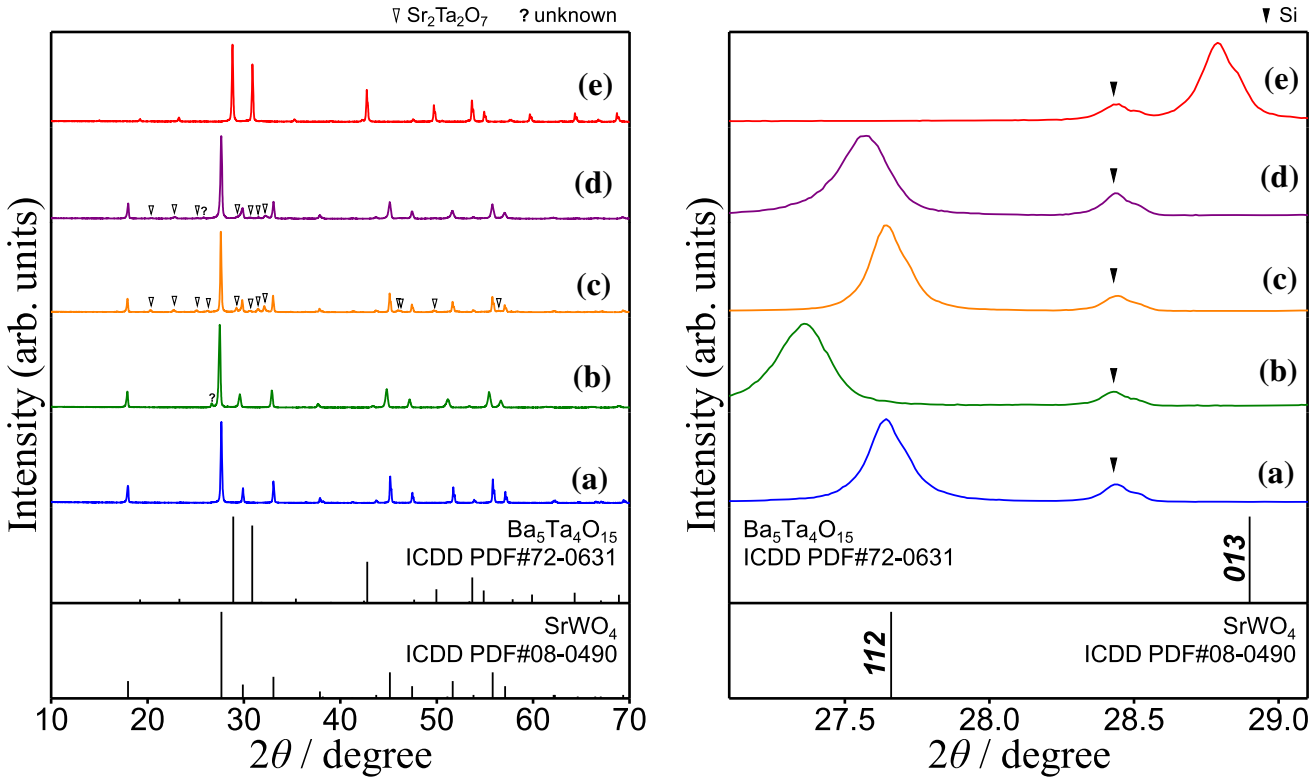

Fig. 1 XRD patterns of $Sr_{1-x}Ba_xW_{1-y}Ta_yO_{4-(1/2)y}$: (*a*) *x*,*y* = 0,0; (*b*) *x*,*y* = 0.25,0; (*c*) *x*,*y* = 0,0.25; (*d*) *x*,*y* = 0.125,0.125; and (*e*) $Ba_5Ta_4O_{15}$ crystals grown by a solid-state reaction and KCl flux method

smaller Sr^{2+} ions (r_{ionic} = 1.26 Å: CN = 8), which is consistent with the Vegard's law for solid solutions [19, 20]. In contrast, for the Ta^{5+}-substitution levels of 0 and 25%, although the W^{6+} may be partially substituted with Ta^{5+}, there is no significant difference between the positions of the main *112* diffraction peaks of the XRD patterns of the synthesized crystals because the ionic radius of W^{6+} is quite similar to that of Ta^{5+} [19]. Nevertheless, an entire amount of tantalum could not be incorporated in the $SrWO_4$ owing to the partial separation of the $Sr_2Ta_2O_7$ phase during the crystal growth process. The lattice constants and unit cell volumes of the $Sr_{1-x}Ba_xW_{1-y}Ta_yO_{4-(1/2)y}$ crystals estimated using the XRD results are listed in Table 1.

Figure 2 shows the UV–Vis diffuse reflectance spectra of the as-synthesized $SrWO_4$, $Sr_{0.75}Ba_{0.25}WO_4$, $SrW_{0.75}Ta_{0.25}O_{3.975}$, $Sr_{0.875}Ba_{0.125}W_{0.875}Ta_{0.125}O_{3.9375}$, and $Ba_5Ta_4O_{15}$ precursor crystals. The $SrWO_4$, $Sr_{0.75}Ba_{0.25}WO_4$, $SrW_{0.75}Ta_{0.25}O_{3.975}$, $Sr_{0.875}Ba_{0.125}W_{0.875}Ta_{0.125}O_{3.9375}$, and $Ba_5Ta_4O_{15}$ crystals have clear absorption edges at about 265, 264, 287, 323, and 281 nm, respectively. The band-gap energies (E_g), estimated by the equation: $E_g = hc/\lambda$, where *h* is the Planck's constant, *c* is the speed of light (m s^{-1}), and λ is the wavelength (nm) [12], are about 4.68 eV for $SrWO_4$, 4.7 eV for $Sr_{0.75}Ba_{0.25}WO_4$, 4.32 eV for $SrW_{0.75}Ta_{0.25}O_{3.975}$, 3.84 eV for $Sr_{0.875}Ba_{0.125}W_{0.875}Ta_{0.125}O_{3.9375}$, and 4.41 eV for $Ba_5Ta_4O_{15}$. The $Sr_{0.75}Ba_{0.25}WO_4$ crystals show a higher band-gap energy compared with the $SrWO_4$ crystals because the electrons belonging to the *A*-site of AWO_4 contribute to the valence (O^{2-} 2*p* states) and conduction bands (W^{6+} 5*d* states) [21]. Lacomba-Perales et al. [21] pointed out that the larger the ionic radius of the A^{2+} cation is, the higher the band-gap energy of the AWO_4 crystals is, which is in good agreement with our results and the previous experimental and theoretical reports on $Ba_{1-x}Sr_xWO_4$ [22, 23]. In comparison with other samples, the $SrW_{0.75}Ta_{0.25}O_{3.975}$ and $Sr_{0.875}Ba_{0.125}W_{0.875}Ta_{0.125}O_{3.9375}$ crystals show lower band-gap energies, although it was previously reported that the band-gap energy of tantalum-doped *hex*-WO_3 was higher than that of pure *hex*-WO_3 due to the Ta^{5+} ions with d^0 electronic configuration [24]. The redshift of the band-

Table 1 Unit cell parameters of tetragonal $Sr_{1-x}Ba_xW_{1-y}Ta_yO_{4-(1/2)y}$ (*x*,*y* = 0,0; 0.25,0; 0,0.25; and 0.125,0.125) crystals grown by a solid-state reaction

(*x*,*y*)	*a* (Å)	*b* (Å)	*V* (Å^3)
(0,0)	5.41605 (83)	11.94920 (367)	350.514 (152)
(0.25,0)	5.46366 (66)	12.11029 (294)	361.511 (124)
(0,0.25)	5.41595 (25)	11.95297 (112)	350.611 (46)
(0.125,0.125)	5.42740 (50)	11.99230 (220)	353.254 (92)

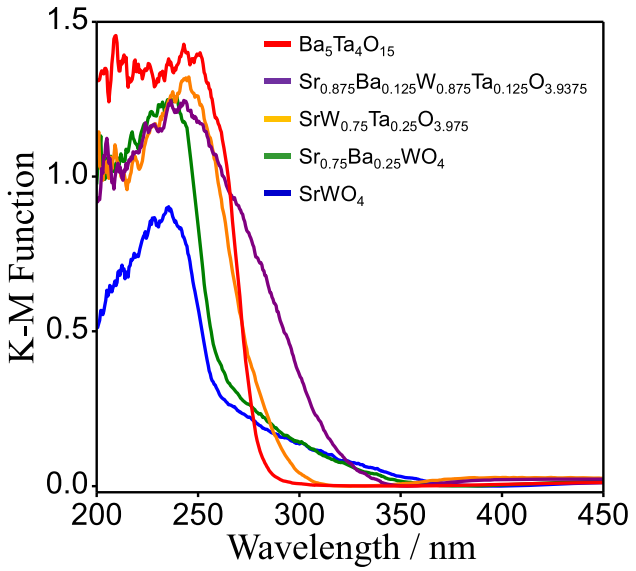

Fig. 2 UV–Vis diffuse reflectance spectra of $Sr_{1-x}Ba_xW_{1-y}Ta_yO_{4-(1/2)y}$: *blue* $x,y = 0,0$; *green* $x,y = 0.25,0$; *orange* $x,y = 0,0.25$; *purple* $x,y = 0.125,0.125$; and *red* $Ba_5Ta_4O_{15}$ crystals grown by a solid-state reaction and KCl flux method

gap energies can be explained by two possibilities: (i) the insertion of the tantalum species (Ta^{5+}) into the Sr^{2+}-$W^{6+}O_4$ crystal lattice generated oxygen vacancies that reduced the band-gap energy of $Sr_{1-x}Ba_xW_{1-y}Ta_yO_{4-(1/2)y}$ [25] and (ii) the W-doped $Sr_2Ta_2O_7$ phase with a narrow band gap was formed during the crystal growth process [26]. The narrow band gap of the W-doped $Sr_2^{2+}Ta_2^{5+}O_7$ was observed because the tungsten (W^{5+} with $5d^1$ electronic configuration) doping increased its electronic density near the conduction band edge and formed the intermediary energy levels in the forbidden band. Interestingly, the $Sr_{0.875}Ba_{0.125}W_{0.875}Ta_{0.125}O_{3.9375}$ crystals show the lowest band-gap energy among all samples, possibly owing to the formation of the Ba-doped $Sr_2Ta_2O_7$ impurity phase that also possesses a lower band-gap energy [27].

The as-synthesized precursor oxides were successfully transformed into the cubic perovskite-type oxynitrides. Figure 3 shows the XRD patterns of the $Sr_{1-x}Ba_xW_{1-y}Ta_yO_{4-(1/2)y}$ and $Ba_5Ta_4O_{15}$ crystals ammonolyzed at 900 and 950 °C for different holding times (10–40 h) under an NH_3 flow. The diffraction lines of the ammonolyzed $Sr_{1-x}Ba_xW_{1-y}Ta_yO_{4-(1/2)y}$ and $Ba_5Ta_4O_{15}$ crystals can be assigned to the cubic perovskite-type $SrWO_{2.05}N_{0.95}$ (ICDD PDF# 88-0828) and $BaTaO_2N$ with space group of *Pm*-3 *m* (ICDD PDF# 84-1748), respectively. During the $Ba_5Ta_4O_{15}$-to-$BaTaO_2N$ conversion, the BaO is typically formed. However, the formation of BaO was not observed here because the volatilization of barium took place during the long thermal ammonolysis:

$$Ba_5Ta_4O_{15} + 4NH_3 \rightarrow 4BaTaO_2N + BaO\uparrow + 6H_2O\uparrow \quad (3)$$

Here, the differences in both the XRD peak shifts and the unit cell parameters (Table 2) of the $Sr_{1-x}Ba_xW_{1-y}Ta_yO_{4-(1/2)y}$ crystal structures can be interpreted by Vegard's law [20]. As shown in Fig. 3a, b, d, e, the *110* diffraction

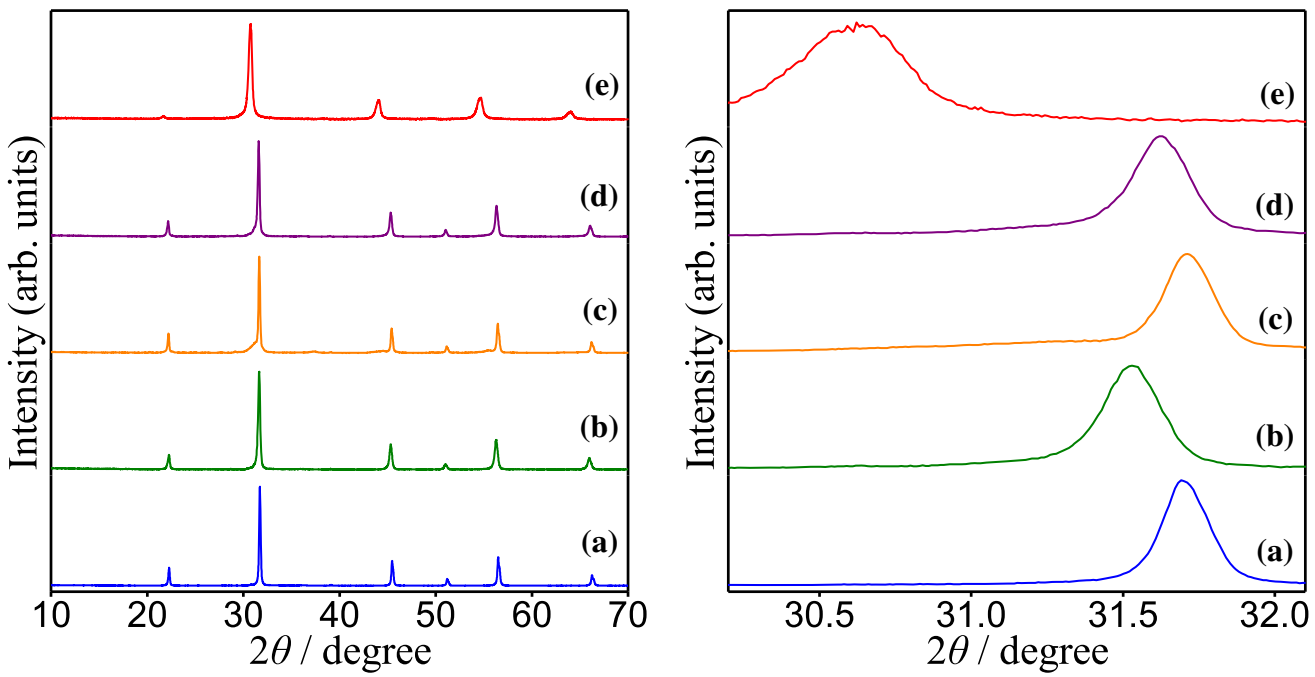

Fig. 3 XRD patterns of $Sr_{1-x}Ba_xW_{1-y}Ta_y(O,N)_3$: (*a*) $x,y = 0,0$; (*b*) $x,y = 0.25,0$; (*c*) $x,y = 0,0.25$; (*d*) $x,y = 0.125,0.125$; and (*e*) $BaTa(O,N)_3$ crystal structures synthesized by thermal ammonolysis of oxide precursors at 900–950 °C for 10–40 h under an NH_3 flow

Table 2 Unit cell parameters of cubic $Sr_{1-x}Ba_xW_{1-y}Ta_y(O,N)_3$ ($x,y = 0,0$; 0.25,0; 0,0.25; and 0.125,0.125) crystal structures synthesized by thermal ammonolysis of oxide precursors at 900–950 °C for 10–40 h under an NH_3 flow

(x,y)	a (Å)	V (Å^3)
(0,0)	3.98799 (44)	63.425 (21)
(0.25,0)	4.00996 (39)	64.479 (19)
(0,0.25)	3.98641 (38)	63.350 (18)
(0.125,0.125)	3.99621 (62)	63.818 (29)
(1,1)	4.11831 (154)	69.849 (79)

peak of the $Sr_{1-x}Ba_xW_{1-y}Ta_y(O,N)_3$ crystal structures at 30.72–31.77° in the XRD patterns shifted slightly to a lower 2θ angle compared with that of the $SrW(O,N)_3$ crystal structures on increasing the level of barium substitution because of an increase in the lattice volume. As the radius of Ba^{2+} ($r_{ionic} = 1.61$ Å: CN = 12) is larger than that of Sr^{2+} ($r_{ionic} = 1.44$ Å: CN = 12), the increase in the unit cell volume indicates that the strontium in cubic perovskite-type $SrW(O,N)_3$ is partially substituted with barium [19]. In spite of the substitution of smaller W^{6+} ($r_{ionic} = 0.6$ Å: CN = 6) and W^{5+} ($r_{ionic} = 0.62$ Å: CN = 6) by larger Ta^{5+} ($r_{ionic} = 0.64$ Å: CN = 6), the $SrW_{0.75}Ta_{0.25}(O,N)_3$ crystal structures have a smaller unit cell volume in comparison with the $SrW(O,N)_3$ crystal structures because the content of N^{3-} ($r_{ionic} = 1.46$ Å: CN = 4), which is larger than that of O^{2-} ($r_{ionic} = 1.36$ Å: CN = 4), was gradually decreased as a consequence of the charge compensation [19]. Based on the obtained results, the effect of the cation and anion substitution on unit cell volume of $Sr_{1-x}Ba_xW_{1-y}Ta_y(O,N)_3$ can be placed in the following order: Sr^{2+}-to-Ba^{2+} > N^{3-}-to-O^{2-} > Ta^{5+}-to-W^{6+} and W^{5+}.

Figure 4 shows the UV–Vis diffuse reflectance spectra of the $Sr_{1-x}Ba_xW_{1-y}Ta_y(O,N)_3$ and $BaTa(O,N)_3$ crystal structures. As the valence band edge of oxynitride is more positive than that of oxide due to the contribution of N 2p orbitals having a more positive potential energy than the O 2p orbitals [12, 28], all the oxynitride crystal structures exhibit visible light absorption. The $SrW(O,N)_3$ and $Sr_{0.75}Ba_{0.25}W(O,N)_3$ crystal structures have an upward shift in absorption in the visible light region (λ = 270–800 nm) with unclear absorption edges, and their color changed to dark taupe, which is attributed to the defects such as oxygen and nitrogen vacancies and reduced tungsten species (W^{5+} and W^{4+}) [12, 13]. According to the theoretical prediction of the formability of the transition metal oxynitrides based on the tolerance and octahedral factors [29], the $AW(O,N)_3$ crystal structures would be formed with the formal compositions of $A^{2+}W^{6+}ON_2$, $A^{2+}W^{5+}O_2N$, and $A^{2+}W^{6+}_{1-x}W^{5+}_xO_{1+x}N_{2-x}$. Furthermore, Yashima et al. [30] reported that the $Ca_xSr_{1-x}WO_2N$ could

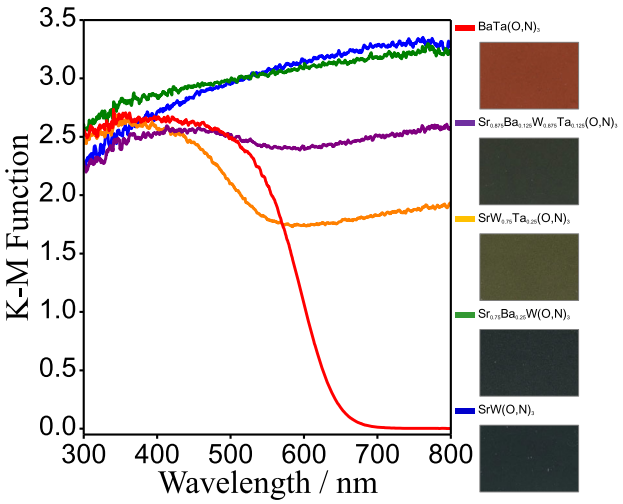

Fig. 4 UV–Vis diffuse reflectance spectra of $Sr_{1-x}Ba_xW_{1-y}Ta_y(O,N)_3$: *blue* $x,y = 0,0$; *gree* $x,y = 0.25,0$; *orange* $x,y = 0,0.25$; *purple* $x,y = 0.125,0.125$; and *red* $BaTa(O,N)_3$ crystal structures synthesized by thermal ammonolysis of oxide precursors at 900–950 °C for 10–40 h under an NH_3 flow

have a black color and metallic characteristics because of the presence of the W^{5+} ion with $5d^1$ electronic configuration. The results obtained in this study are consistent with the previously reported theoretical and experimental data. As shown in Fig. 4, the absorption edges of the dark olive-colored $SrW_{0.75}Ta_{0.25}(O,N)_3$, dark viridian-colored $Sr_{0.875}Ba_{0.125}W_{0.875}Ta_{0.125}(O,N)_3$, and brown-colored $BaTa(O,N)_3$ crystal structures are confirmed to be at 557, 581, and 645 nm, respectively. On the contrary to $SrW(O,N)_3$ and $Sr_{0.75}Ba_{0.25}W(O,N)_3$, the light absorption of $SrW_{0.75}Ta_{0.25}(O,N)_3$ and $Sr_{0.875}Ba_{0.125}W_{0.875}Ta_{0.125}(O,N)_3$ beyond 560 and 580 nm is weakened. This indicates that the lower absorption in the near-infrared region stems from the suppression of the generation of the reduced W^{5+} and W^{4+} ions with $5d^1$ and $5d^2$ electronic configuration during thermal ammonolysis due to the partial substitution of *B*-site with Ta^{5+} having $5d^0$ electronic configuration. Here, the band gap shifted from 2.23 eV for $SrW_{0.75}Ta_{0.25}(O,N)_3$ to 2.13 eV for $Sr_{0.875}Ba_{0.125}W_{0.875}Ta_{0.125}(O,N)_3$ and 1.92 eV for $BaTa(O,N)_3$. The O and N were quantitatively analyzed and found to be in the following stoichiometric compositions in the samples: $SrWO_{2.15}N_{0.85}$, $Sr_{0.75}Ba_{0.25}WO_{2.37}N_{0.63}$, $SrW_{0.75}Ta_{0.25}O_{2.52}N_{0.48}$, $Sr_{0.875}Ba_{0.125}W_{0.875}Ta_{0.125}O_{2.31}N_{0.69}$, and $BaTaO_{2.45}N_{0.55}$. The discrepancy between the band-gap energies of $SrW_{0.75}Ta_{0.25}(O,N)_3$, $Sr_{0.875}Ba_{0.125}W_{0.875}Ta_{0.125}(O,N)_3$, and $BaTa(O,N)_3$ can be explained by both the effects of *A*- and *B*-site cation change and variation in the oxygen/nitrogen ratio among the synthesized oxynitrides. In previous reports on ABO_2N (A = Ca, Sr, Ba; B = Ta, Nb), it was proposed that the band-gap energies of ABO_2N can be narrowed by increasing the ionic radius of A^{2+}

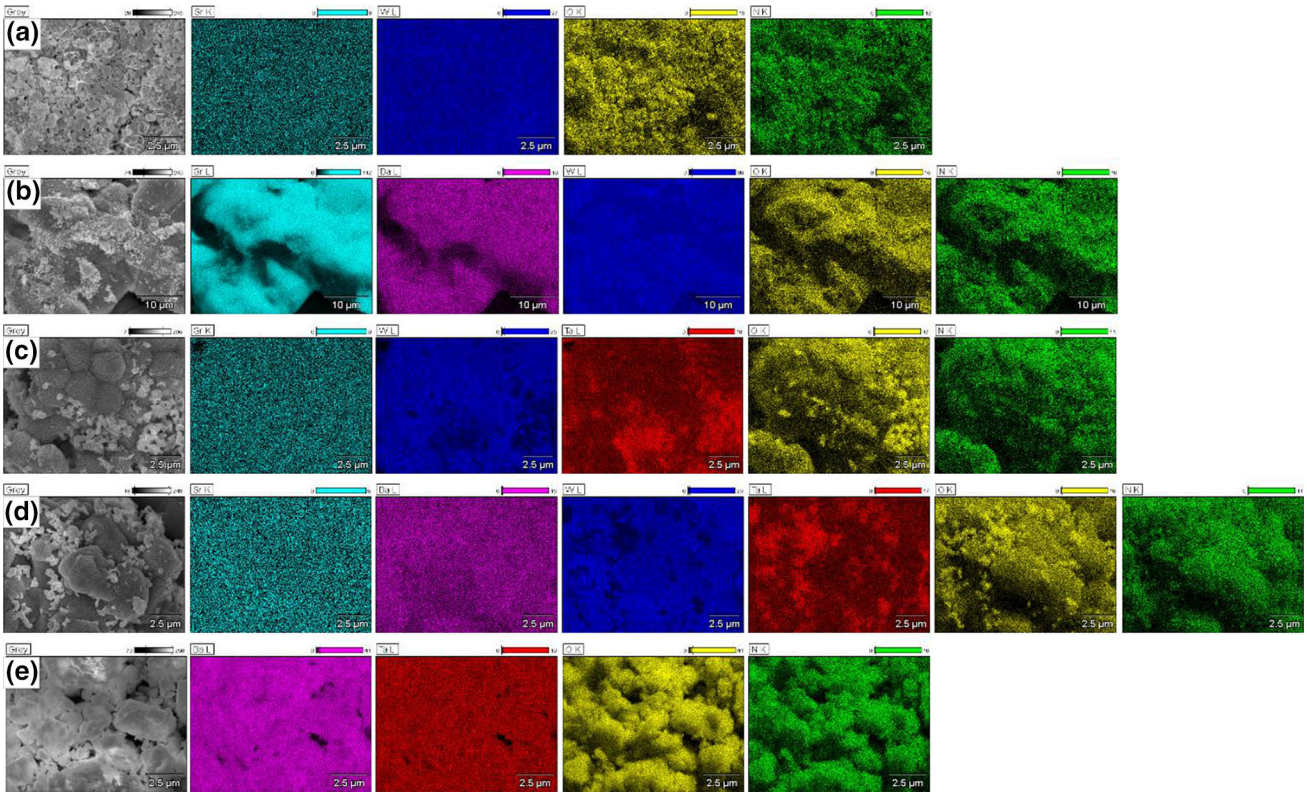

Fig. 5 EDS element mapping images of $Sr_{1-x}Ba_xW_{1-y}Ta_y(O,N)_3$: (*a*) *x*,*y* = 0,0; (*b*) *x*,*y* = 0.25,0; (*c*) *x*,*y* = 0,0.25; (*d*) *x*,*y* = 0.125,0.125; and (*e*) $BaTa(O,N)_3$ crystal structures obtained by thermal ammonolysis of oxide precursors at 900–950 °C for 10–40 h under an NH_3 flow

($Ca^{2+} < Sr^{2+} < Ba^{2+}$) [31–33]. Moreover, Ikeda et al. [34] proposed that since the potential of W 5*d* orbitals is located at a more negative potential than that of Ta 5*d* orbitals, the conduction band energy level of tantalum-containing tungsten-based materials is more positive compared to tungsten-based materials. The $Sr_{0.875}Ba_{0.125}W_{0.875}Ta_{0.125}(O,N)_3$ crystal structures exhibited a narrower band-gap energy than the $SrW_{0.75}Ta_{0.25}(O,N)_3$ crystal structures due to the partial replacement of smaller Sr^{2+} by larger Ba^{2+}, lower Ta^{5+}-substitution level, and higher nitrogen concentration in $Sr_{0.875}Ba_{0.125}W_{0.875}Ta_{0.125}(O,N)_3$. Although the Ta-based $BaTa(O,N)_3$ crystal structures have a lower concentration of nitrogen than the $Sr_{0.875}Ba_{0.125}W_{0.875}Ta_{0.125}(O,N)_3$ crystal structures, their band-gap energy was found to be the smallest one among the five samples, resulting from the effect of Ba^{2+}.

The EDS element mapping images are shown in Fig. 5. The strontium (*cyan*), barium (*purple*), oxygen (*yellow*), and nitrogen (*green*) elements are uniformly distributed over the $SrW(O,N)_3$, $Sr_{0.75}Ba_{0.25}W(O,N)_3$, $SrW_{0.75}Ta_{0.25}(O,N)_3$, $Sr_{0.875}Ba_{0.125}W_{0.875}Ta_{0.125}(O,N)_3$, and $BaTa(O,N)_3$ crystal structures, implying that the strontium and oxygen were partially substituted by barium and nitrogen in the $SrW(O,N)_3$ lattice. However, the lower intensity of tungsten (*blue*) signal and higher intensity of tantalum (*red*) signal are observed in the regions of a few microns in the $SrW_{0.75}Ta_{0.25}(O,N)_3$ and $Sr_{0.875}Ba_{0.125}W_{0.875}Ta_{0.125}(O,N)_3$ crystal structures which are probably related to the ammonolyzed $Sr_2Ta_2O_7$ crystals ($SrTaO_2N$). All the results of the EDS element mapping images are consistent with the EDS spectra shown in the Supporting Information (Fig. S3).

Photocatalytic water oxidation activities of $Sr_{1-x}Ba_xW_{1-y}Ta_y(O,N)_3$ crystal structures

The as-synthesized oxynitrides were tested as visible light-active photocatalysts for water oxidation half-reaction in the presence of Ag^+ as a sacrificial electron acceptor that prevents the H_2 evolution reaction, avoids the H_2O-forming back reaction ($H_2 + 1/2O_2 \rightarrow H_2O$), and enhances the O_2 evolution reaction [35]. Figure 6 shows the time course curves of O_2 and N_2 evolution over the as-synthesized oxynitrides loaded with CoO_x (2 wt % Co) nanoparticles and suspended in aqueous $AgNO_3$ solution under visible light irradiation ($\lambda > 420$ nm). The loaded CoO_x nanoparticles as a cocatalyst for photocatalytic water oxidation can trap photo-generated holes to separate effectively the photo-excited charges using a cocatalyst/photocatalyst interface and to improve the photocatalytic

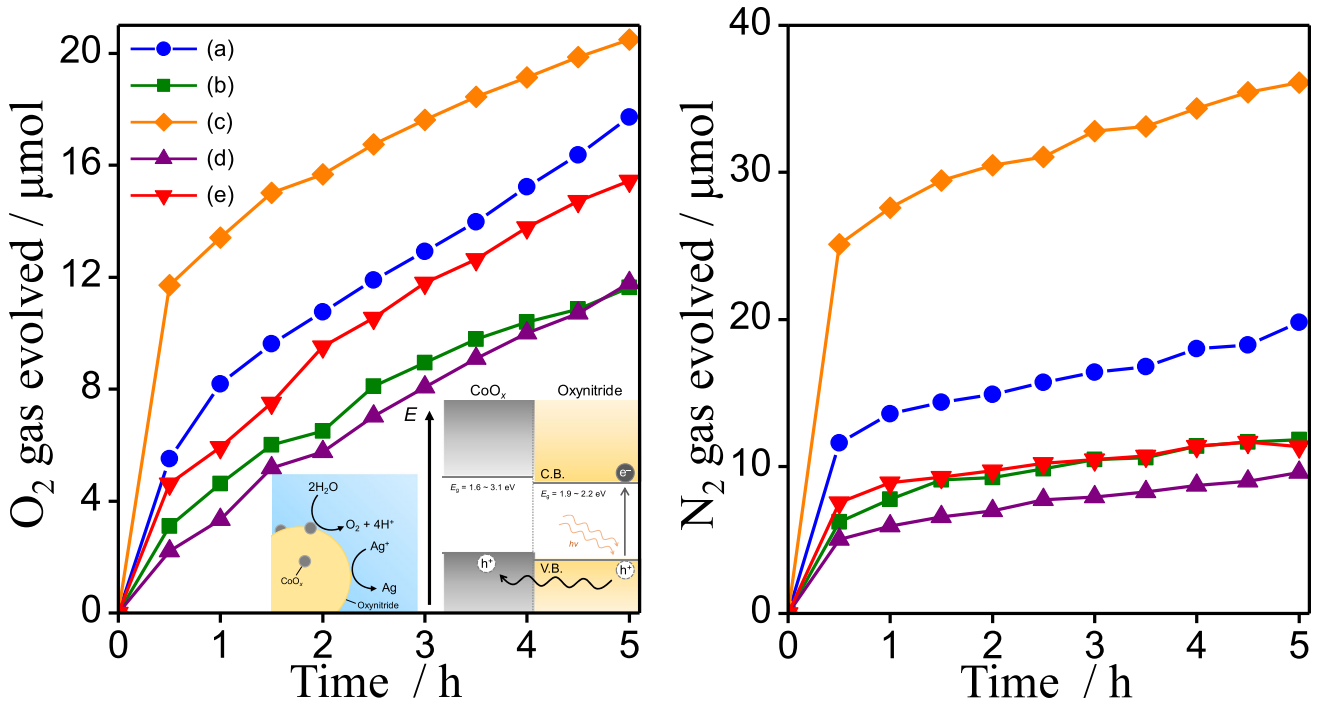

Fig. 6 O_2 and N_2 evolution of CoO_x-loaded $Sr_{1-x}Ba_xW_{1-y}Ta_y(O,N)_3$: (*a*) $x,y = 0,0$; (*b*) $x,y = 0.25,0$; (*c*) $x,y = 0,0.25$; (*d*) $x,y = 0.125,0.125$; and (*e*) $BaTa(O,N)_3$ crystal structures obtained by thermal ammonolysis of oxide precursors at 900–950 °C for 10–40 h under an NH_3 flow in the presence of a sacrificial reagent ($AgNO_3$)

performance. The corresponding photocatalytic reactions are schematically illustrated in the insets of Fig. 6 [7, 36–38]. The detected O_2 gas was evolved as a result of the oxidation of H_2O to O_2 by photo-generated holes on CoO_x nanoparticles:

$$4AgNO_3 + 2H_2O \rightarrow 4Ag + 4HNO_3 + O_2 \uparrow \quad (4)$$

The TONs and TOFs estimated for 5 h photocatalytic O_2 evolution reactions are given in Table 3. Generally, a TON of less than one does not confirm the existence of catalysis [39]. Since the resultant TONs of all the samples exceed one, the observed O_2 gas evolution reactions are catalytic. Here, the N_2 gas evolution was also noticed because the nitrogen anions (N^{3-}) in the as-synthesized oxynitride crystal structures are self-oxidized to N_2 by photo-generated holes:

$$2N^{3-} + 6h^+ \rightarrow N_2 \uparrow \quad (5)$$

Simultaneously, the highly resistive oxides ($Sr_{1-x}Ba_xW_{1-y}Ta_yO_{4-(1/2)y}$) were also formed on the oxynitride surface due to the self-oxidation, hindering the transport of the photo-generated charge carriers from the inside of the crystals to the interface between the crystal and reaction solution [40, 41]. As shown in Fig. 6, all the O_2 evolution rates drastically decreased over time, especially after 0.5 h, because of two possible reasons: (i) the self-oxidative formation of the highly resistive oxides and (ii) photo-deposition of metallic silver nanoparticles on the oxynitride crystal surfaces [42]. Here, the metallic silver nanoparticles disturb light absorption and cover surface active sites.

Table 3 Photocatalytic performance of CoO_x-loaded $Sr_{1-x}Ba_xW_{1-y}Ta_y(O,N)_3$ ($x,y = 0,0$; 0.25,0; 0,0.25; and 0.125,0.125) on water oxidation and specific surface areas of $Sr_{1-x}Ba_xW_{1-y}Ta_y(O,N)_3$ crystal structures

Sample name	TON	TOF (h^{-1})	O_2 evolution rate (μmol h^{-1}) within the first 0.5 h	S_{BET} ($m^2 \cdot g^{-1}$)
SWON	2.10	0.421	11.0	5.7
SBWON	1.38	0.276	6.22	5.4
SWTON	2.43	0.487	23.4	14.7
SBWTON	1.40	0.280	4.43	6.6
BTON	1.83	0.367	9.22	14.1

The CoO_x-loaded $SrW(O,N)_3$ (CoO_x-SWON), $Sr_{0.75}Ba_{0.25}W(O,N)_3$ (CoO_x-SBWON), $SrW_{0.75}Ta_{0.25}(O,N)_3$ (CoO_x-SWTON), $Sr_{0.875}Ba_{0.125}W_{0.875}Ta_{0.125}(O,N)_3$ (CoO_x-SBWTON), and $BaTa(O,N)_3$ (CoO_x-BTON) crystal structures exhibited the total amounts of evolved gases: 17.7, 11.6, 20.5, 11.8, and 15.4 μmol for O_2 gas and 19.8, 11.8, 36.1, 9.6, and 11.3 μmol for N_2 gas, respectively. CoO_x-SWTON demonstrated nearly a 1.2-fold higher amount of evolved O_2 gas compared to the CoO_x-SWON because of its higher specific surface area and lower concentration of

intrinsic defects (W^{5+}) owing to the partial substitution of Ta^{5+} for W^{6+} prompting the oxidation of tungsten. However, the total amounts of evolved O_2 gas over CoO_x-SBWON, CoO_x-SBWTON, and CoO_x-BTON were much lower than that of CoO_x-SWON. According to previous reports on nitrogen-doped tungsten oxide [43, 44], the doping of nitrogen onto the WO_6 octahedra in WO_3 changes the bond overlap population of W–O leading to the lattice distortion. In addition, Wang et al. [45] revealed that a large lattice distortion of the corner-linked BO_6 octahedra in the $A_2B_2O_7$-type photocatalyst induces the high photocatalytic activity. Therefore, when the nitrogen content of the as-synthesized $AB(O,N)_3$-type oxynitrides is higher, the distortion of the BO_6 octahedra (B = W and/or Ta) is expected to become larger, leading to the higher photocatalytic activity. As the nitrogen content of $SrW(O,N)_3$ was much higher than that of $SrW_{0.75}Ta_{0.25}(O,N)_3$, $Sr_{0.875}Ba_{0.125}W_{0.875}Ta_{0.125}(O,N)_3$, and $BaTa(O,N)_3$, the CoO_x-SWON showed the highest water oxidation activity among the four samples. From the EDS and XPS results (see Fig. S4 in the Supporting Information), it was found that the $SrW_{0.75}Ta_{0.25}(O,N)_3$ and $Sr_{0.875}Ba_{0.125}W_{0.875}Ta_{0.125}(O,N)_3$ crystal structures contain strontium tantalum oxynitride as a secondary phase. As is known, the strontium tantalum oxynitride has the photocatalytic activity for water oxidation half-reaction under visible light irradiation [46]. Possibly, the secondary phase can provide a positive effect on the O_2 evolution reaction. Additionally, the XPS results (see Fig. S4 in the Supporting Information) show that the crystal surfaces of all the synthesized oxynitrides may be partially covered with the metallic tungsten and compounds containing low-valent transition metal cations (e.g., W, WO_2, W_2N, TaO_2, etc.). In general, the compounds with low-valent transition metal cations have metallic characteristics due to the partially filled d orbitals [30, 47–49]. Furthermore, the compounds with the fully/partially filled d orbitals are expected to act as a cocatalyst accepting the photo-generated electrons [50]. The total amount of evolved O_2 and N_2 increases in the following order: CoO_x-SWTON > CoO_x-SWON > CoO_x-BTON > CoO_x-SBWON > CoO_x-SBWTON, giving a close agreement with the order of the TOF and initial O_2 evolution rate shown in Table 3. Noticeably, both O_2 and N_2 gas evolution amounts certainly depend on the number of photo-generated carriers arriving near the crystal surfaces. Hence, it is concluded that the partial Ta^{5+}-to-$W^{4\sim6+}$ substitution is most effective in enhancing the photocatalytic activity of $SrW(O,N)_3$. The photocatalytic water oxidation activities of the $Sr_{1-x}Ba_xW_{1-y}Ta_y(O,N)_3$ (x,y = 0,0; 0.25,0; 0.125,0.125; 0,0.25; and 1,1) crystal structures can be further improved by enhancing their photostability during the photocatalytic reaction.

Conclusion

In summary, $SrW(O,N)_3$ crystal structures with fully/partially substituted Ba^{2+} and/or Ta^{5+} were synthesized by thermal ammonolysis of their corresponding oxide precursors $Sr_{1-x}Ba_xW_{1-y}Ta_yO_{4-(1/2)y}$ (x,y = 0,0; 0.25,0; 0,0.25; and 0.125,0.125) and $Ba_5Ta_4O_{15}$. The synthesized oxynitrides possess porous structures with higher specific surface areas. In the photocatalytic water oxidation activity test, the estimated TONs of the oxynitride samples exceeded one, evidencing that the observed O_2 gas evolution reactions were catalytic. The CoO_x-loaded $SrW_{0.75}Ta_{0.25}(O,N)_3$ showed a comparatively higher O_2 gas evolution activity compared to CoO_x-loaded $SrW(O,N)_3$ because of its relatively higher specific surface area and lower concentration of intrinsic defects. Therefore, the partial Ta^{5+}-to-$W^{4\sim6+}$ substitution is most effective for enhancing the activity of $SrWO_2N$ photocatalyst. After the initial 0.5 h reaction, the O_2 gas evolution rate decreased dramatically due to the self-oxidation of the surfaces of the oxynitride crystals, forming the highly resistive oxides, and the photo-deposition of metallic silver nanoparticles on the oxynitride crystal surfaces, disturbing light absorption and cover surface active sites. Further improvement of the photocatalytic activity for water oxidation of the $Sr_{1-x}Ba_xW_{1-y}Ta_y(O,N)_3$ is in process.

Acknowledgements This research was supported in part by the Japan Technological Research Association of Artificial Photosynthetic Chemical Process (ARPChem). The authors thank Ms. Reiko Shiozawa for her kind assistance in XPS measurement.

References

1. Chen, X., Shen, S., Guo, L., Mao, S.S.: Semiconductor-based photocatalytic hydrogen generation. Chem. Rev. **110**, 6503–6570 (2010)
2. Connelly, K., Wahab, A.K., Idriss, H.: Photoreaction of Au/TiO_2 for hydrogen production from renewables: a review on the synergistic effect between anatase and rutile phases of TiO_2. Mater. Renew. Sustain. Energy **1**, 1–12 (2012)
3. Nurlaela, E., Ziani, A., Takanabe, K.: Tantalum nitride for photocatalytic water splitting: concept and applications. Mater. Renew. Sustain. Energy **5**, 18 (2016)
4. Navarro Yerga, R.M., Álvarez Galván, M.C., Del Valle, F., Villoria de la Mano, J.A., Fierro, J.L.: Water splitting on

semiconductor catalysts under visible-light irradiation. Chemsuschem **2**, 471–485 (2009)
5. Maeda, K., Domen, K.: New non-oxide photocatalysts designed for overall water splitting under visible light. J. Phys. Chem. C **111**, 7851–7861 (2007)
6. Maeda, K.: (Oxy)nitrides with d^0-electronic configuration as photocatalysts and photoanodes that operate under a wide range of visible light for overall water splitting. Phys. Chem. Chem. Phys. **15**, 10537–10548 (2013)
7. Zhang, F., Yamakata, A., Maeda, K., Moriya, Y., Takata, T., Kubota, J., Teshima, K., Oishi, S., Domen, K.: Cobalt-modified porous single-crystalline $LaTiO_2N$ for highly efficient water oxidation under visible light. J. Am. Chem. Soc. **134**, 8348–8351 (2012)
8. Hisatomi, T., Katayama, C., Moriya, Y., Minegishi, T., Katayama, M., Nishiyama, H., Yamada, T., Domen, K.: Photocatalytic oxygen evolution using $BaNbO_2N$ modified with cobalt oxide under photoexcitation up to 740 nm. Energy Environ. Sci. **6**, 3595–3599 (2013)
9. Higashi, M., Domen, K., Abe, R.: Fabrication of an efficient $BaTaO_2N$ photoanode harvesting a wide range of visible light for water splitting. J. Am. Chem. Soc. **135**, 10238–10241 (2013)
10. Xu, J., Pan, C., Takata, T., Domen, K.: Photocatalytic overall water splitting on the perovskite-type transition metal oxynitride $CaTaO_2N$ under visible light irradiation. Chem. Commun. **51**, 7191–7194 (2015)
11. Pan, Z., Hisatomi, T., Wang, Q., Chen, S., Nakabayashi, M., Shibata, N., Pan, C., Takata, T., Katayama, M., Minegishi, T., Kudo, A., Domen, K.: Photocatalyst sheets composed of particulate $LaMg_{1/3}Ta_{2/3}O_2N$ and Mo-doped $BiVO_4$ for z-scheme water splitting under visible light. ACS Catal. **6**, 7188–7196 (2016)
12. Kawashima, K., Hojamberdiev, M., Wagata, H., Zahedi, E., Yubuta, K., Domen, K., Teshima, K.: Two-step synthesis and visible-light-driven photocatalytic water oxidation activity of AW(O, N)3 (A = Sr, La, Pr, Nd and Eu) perovskites. J. Catal. **344**, 29–37 (2016)
13. Maegli, A.E., Hisatomi, T., Otal, E.H., Yoon, S., Pokrant, S., Grätzel, M., Weidenkaff, A.: Structural and photocatalytic properties of perovskite-type (La, Ca)Ti(O, N)3 prepared from A-site deficient precursors. J. Mater. Chem. **22**, 17906–17913 (2012)
14. Masuda, Y., Mashima, R., Yamada, M., Ikeuchi, K., Murai, K., Waterhouse, G.I.N., Metson, J.B., Moriga, T.: Relationship between anion and cation nonstoichiometries and valence state of titanium in perovskite-type oxynitrides $LaTiO_2N$. J. Ceram. Soc. Jpn. **117**, 76–81 (2009)
15. Maeda, K., Lu, D., Domen, K.: Oxidation of water under visible-light irradiation over modified $BaTaO_2N$ photocatalysts promoted by tungsten species. Angew. Chem. Int. Ed. **52**, 6488–6491 (2013)
16. Hojamberdiev, M., Bekheet, M.F., Zahedi, E., Wagata, H., Vequizo, J.J.M., Yamakata, A., Yubuta, K., Gurlo, A., Domen, K., Teshima, K.: The contrasting effect of the Ta/Nb ratio in (111)-layered *B*-site deficient hexagonal perovskite $Ba_5Nb_{4-x}Ta_xO_{15}$ crystals on visible-light-induced photocatalytic water oxidation activity of their oxynitride derivatives. Dalton Trans. **45**, 12559–12568 (2016)
17. Ohtani, B.: Revisiting the fundamental physical chemistry in heterogeneous photocatalysis: its thermodynamics and kinetics. Phys. Chem. Chem. Phys. **16**, 1788–1797 (2014)
18. Ohtani, B.: Photocatalyst. In: Kreysa, G., Ota, K., Savinell, R.F. (eds.) Encyclopedia of applied electrochemistry, pp. 1529–1532. Springer, New York (2014)
19. Shannon, R.T.: Revised effective ionic radii and systematic studies of interatomic distances in halides and chalcogenides. Acta Crystallogr. A **32**, 751–767 (1976)
20. Denton, A., Ashcroft, N.: Vegard's law. Phys. Rev. A **43**, 3161–3164 (1991)
21. Lacomba-Perales, R., Ruiz-Fuertes, J., Errandonea, D., Martínez-García, D., Segura, A.: Optical absorption of divalent metal tungstates: correlation between the band-gap energy and the cation ionic radius. Eur. Lett. **83**, 37002 (2008)
22. Priya, A., Sinha, E., Rout, S.K.: Structural, optical and microwave dielectric properties of $Ba_{1-x}Sr_xWO_4$ ceramics prepared by solid state reaction route. Solid State Sci. **20**, 40–45 (2013)
23. Haddouch, M.A., Aharbil, Y., Tamraoui, Y., Manoun, B., Lazor, P., Benmokhtar, S.: Synthesis, X-ray diffraction, raman spectroscopy and electronic structure studies of $(Ba_{1-x}Sr_x)WO_4$ ceramics. J. Mater. Environ. Sci. **6**, 3403–3415 (2015)
24. Li, X., Mu, W., Xie, X., Liu, B., Tang, H., Zhou, G., Wei, H., Jian, Y., Luo, S.: Strontium adsorption on tantalum-doped hexagonal tungsten oxide. J. Hazard. Mater. **264**, 386–394 (2014)
25. Migas, D.B., Shaposhnikov, V.L., Rodin, V.N., Borisenko, V.E.: Tungsten oxides. I. Effects of oxygen vacancies and doping on electronic and optical properties of different phases of WO_3. J. Appl. Phys. **108**, 093713 (2010)
26. Liu, P., Nisar, J., Ahuja, R., Pathak, B.: Layered perovskite $Sr_2Ta_2O_7$ for visible light photocatalysis: a first principles study. J. Phys. Chem. C **117**, 5043–5050 (2013)
27. Kim, K.Y., Eun, T.H., Lee, S.S., Chon, U.: Photocatalytic activities and structural changes of barium-doped strontium tantalate. Resour. Process. **56**, 138–144 (2009)
28. Hitoki, G., Takata, T., Kondo, J.N., Hara, M., Kobayashi, H., Domen, K.: An oxynitride, TaON, as an efficient water oxidation photocatalyst under visible light irradiation ($\lambda \leq 500$ nm). Chem. Commun. **16**, 1698–1699 (2002)
29. Li, W., Ionescu, E., Riedel, R., Gurlo, A.: Can we predict the formability of perovskite oxynitrides from tolerance and octahedral factors? J. Mater. Chem. A **1**, 12239–12245 (2013)
30. Yashima, M., Fumi, U., Nakano, H., Omoto, K., Hester, J.R.: Crystal structure, optical properties, and electronic structure of calcium strontium tungsten oxynitrides $Ca_xSr_{1-x}WO_2N$. J. Phys. Chem. C **117**, 18529–18539 (2013)
31. Kim, Y.I., Woodward, P.M., Baba-Kishi, K.Z., Tai, C.W.: Characterization of the structural, optical, and dielectric properties of oxynitride perovskites AMO_2N (A = Ba, Sr, Ca, M = Ta, Nb). Chem. Mater. **16**, 1267–1276 (2004)
32. Wolff, H., Dronskowski, R.: First-principles and molecular-dynamics study of structure and bonding in perovskite-type oxynitrides ABO_2N (A = Ca, Sr, Ba, B = Ta, Nb). J. Comput. Chem. **29**, 2260–2267 (2008)
33. Higashi, M., Abe, R., Takata, T., Domen, K.: Photocatalytic overall water splitting under visible light using $ATaO_2N$ (A = Ca, Sr, Ba) and WO_3 in a IO^{3-}/I^- shuttle redox mediated system. Chem. Mater. **21**, 1543–1549 (2009)
34. Ikeda, S., Itani, T., Nango, K., Matsumura, M.: Overall water splitting on tungsten-based photocatalysts with defect pyrochlore structure. Catal. Lett. **98**, 229–233 (2004)
35. Wang, D., Pierre, A., Kibria, M.G., Cui, K., Han, X., Bevan, K.H., Guo, H., Paradis, S., Hakima, A.R., Mi, Z.: Wafer-level photocatalytic water splitting on GaN nanowire arrays grown by molecular beam epitaxy. Nano Lett. **11**, 2353–2357 (2011)
36. Nurlaela, E., Wang, H., Shinagawa, T., Flanagan, S., Ould-Chikh, S., Qureshi, M., Mics, Z., Sautet, P., Bahers, T.L., Cánovas, E., Bonn, M., Takanabe, K.: Enhanced kinetics of hole transfer and electrocatalysis during photocatalytic oxygen evolution by cocatalyst tuning. ACS Catal. **6**, 4117–4126 (2016)
37. Van Elp, J., Wieland, J.L., Eskes, H., Kuiper, P., Sawatzky, G.A., De Groot, F.M.F., Turner, T.S.: Electronic structure of CoO, Li-doped CoO, and $LiCoO_2$. Phys. Rev. B **44**, 6090 (1991)

38. Shinde, V.R., Mahadik, S.B., Gujar, T.P., Lokhande, C.D.: Supercapacitive cobalt oxide (Co_3O_4) thin films by spray pyrolysis. Appl. Surf. Sci. **252**, 7487–7492 (2006)
39. Childs, L.P., Ollis, D.F.: Is photocatalysis catalytic? J. Catal. **66**, 383–390 (1980)
40. Maeda, K., Higashi, M., Siritanaratkul, B., Abe, R., Domen, K.: $SrNbO_2N$ as a water-splitting photoanode with a wide visible-light absorption band. J. Am. Chem. Soc. **133**, 12334–12337 (2011)
41. Zhong, M., Hisatomi, T., Sasaki, Y., Suzuki, S., Teshima, K., Nakabayashi, M., Shibata, N., Nishiyama, H., Katayama, M., Yamada, T., Domen, K.: Highly active GaN-stabilized Ta_3N_5 thin-film photoanode for solar water oxidation. Angew. Chem. Int. Ed. **56**, 4739–4743 (2017)
42. Kawashima, K., Hojamberdiev, M., Wagata, H., Nakayama, M., Yubuta, K., Oishi, S., Domen, K., Teshima, K.: Amount of tungsten dopant influencing the photocatalytic water oxidation activity of $LaTiO_2N$ crystals grown directly by an NH_3-assisted flux method. Catal. Sci. Technol. **6**, 5389–5396 (2016)
43. Nakagawa, K., Miura, N., Matsumoto, S., Nakano, R., Matsumoto, H.: Electrochromism and electronic structures of nitrogen doped tungsten oxide thin films prepared by RF reactive sputtering. Jpn. J. Appl. Phys. **47**, 7230 (2008)
44. Sun, X., Liu, Z., Cao, H.: Electrochromic properties of N-doped tungsten oxide thin films prepared by reactive DC-pulsed sputtering. Thin Solid Films **519**, 3032–3036 (2011)
45. Wang, J., Zou, Z., Ye, J.: Surface modification and photocatalytic activity of distorted pyrochlore-type Bi_2M(M = In, Ga and Fe)TaO_7 photocatalysts. J. Phys. Chem. Solids **66**, 349–355 (2005)
46. Zhong, Y., Li, Z., Zhao, X., Fang, T., Huang, H., Qian, Q., Chang, X., Wang, P., Yan, S., Yu, Z., Zou, Z.: Enhanced water-splitting performance of perovskite $SrTaO_2N$ photoanode film through ameliorating interparticle charge transport. Adv. Funct. Mater. **26**, 7156–7163 (2016)
47. Liu, Z., Bando, Y., Tang, C.: Synthesis of tungsten oxide nanowires. Chem. Phys. Lett. **372**, 179–182 (2003)
48. Chakrapani, V., Thangala, J., Sunkara, M.K.: WO_3 and W_2N nanowire arrays for photoelectrochemical hydrogen production. Int. J. Hydrog. Energy **34**, 9050–9059 (2009)
49. Zhu, L., Zhou, J., Guo, Z., Sun, Z.: Realization of a reversible switching in TaO_2 polymorphs via Peierls distortion for resistance random access memory. Appl. Phys. Lett. **106**, 091903 (2015)
50. Wang, S., Mak, Y.L., Wang, S., Chai, J., Pan, F., Foo, M.L., Chen, W., Wu, K., Xu, G.Q.: Visible-near-infrared-light-driven oxygen evolution reaction with noble-metal-free WO_2–WO_3 hybrid nanorods. Langmuir **32**, 13046–13053 (2016)